Development of a Novel Flight Time Matrix for Nondestructive Evaluation Using Acousto-Ultrasonics -A Case Study of Multilayered Armor Plates Damage Detection

Stephen James Tankersley and Gang Qi *

Posted Date: 31 October 2023

doi: 10.20944/preprints202310.2048.v1

Keywords: Armor plate; Acoustic emission; Ultrasonics; Nondestructive test

Article

Development of a Novel Flight Time Matrix for Nondestructive Evaluation Using Acousto-Ultrasonics—A Case Study of Multilayered Armor Plates Damage Detection

Stephen James Tankersley [1] and Gang Qi [2,*]

[1] Department of Mechanical Engineering, University of Memphis, Memphis, TN, USA; stankersley@memphis.edu
[2] School of Mechatronic Engineering, Xi'an Technological University, Xi'an, China
* Correspondence: qigang@taut.edu.cn

Abstract: Non-destructive testing is an emerging need in manufacturing processes and in service of ballistic armor plates. It has been shown that acoustic emission and ultrasonics are among the most applicable techniques. However, these techniques often require relative sophisticated processing and strong tech background for the evaluators. The purpose of the present work is to develop a flight time based algorithm and to demonstrate this algorithm using commercial multilayered armor plates. We proposed a novel concept of flight time matrix (FTM). In this work, the proposed FTM was verified first numerically. The numerical simulation revealed perfect results which showed that FTM can be used to assist the nondestructive evaluation of ballistic armor plates using acousto-ultrasonics. Two donated commercial ballistic armor plates were sought for a case study where artificial defects were prepared. The results of FTM were reasonably well. The artificial defects were clearly identifiable in one directional location array and FTM contour graphs. More comprehensive superimpositions of flight time vs location and FTM contour plots can be advanced to a better visualization of the defect presence. The resolution of FTM method is in the range of submillimeter or less. This study demonstrated that AU (acousto-ultrasonics) technique is a field applicable and yet reliable tool for inspection of the hidden defects in body armors. A broader merit of the proposed FTM algorithm is that it may promote the development of specific tools/device for nondestructive evaluations field.

Keywords: armor plate; acoustic emission; ultrasonics; nondestructive test

1. Introduction

Non-destructive evaluation of ballistic body armor plates is an emerging need both in the manufacturing processes and in service because it is the last defense of life saving in a battle field. Issues involved in the integrity and reliability evaluation of these plates include defects, delamination, cracks, and other structural integrity that make an armor plate to be defective. Occurrence of defective plate can be resulted in a number of circumferences such as from manufacturing processes, through rough service, and mishandling [1,2]. The existence of defects will lessen the ability of ballistic protection that armor plates may become compromised. In cases where the compromised plates may have shown that they are able to resist a threat [3], the level of protection is very difficult to determine therefore any damage to armor plates results in its withdrawal from service [4].

Body armor plates used in the field are classified in the forms of soft armors (Type I & II), hard armor (Type III), and multilayer armor (Type IV) [5]. Types I and II are mainly Kevlar based structures, which is a heat-resistant para-aramid synthetic fiber with a molecular structure of many inter-chain bonds that make it incredibly strong. They can protect against the threats of bullets with

 doi:10.20944/preprints202310.2048.v1

velocity < 350 m/s, which includes most of handguns and some rifles. Type III has mixed structures of material layers with Kevlar and metals, which could resist bullets at a velocity up to 847 m/s. Type IV is made of ceramic, Kevlar, metal, and composites with armor-piercing which can resist bullets at a velocity of 878 m/s or higher, which are thus widely used in the military. In the present work, we will concentrate on damage detection and evaluation of Type IV body armor plates.

For years, various nondestructive methods were explored. X-ray [6–8], acoustic emission (AE) [9,10], ultrasonics [7,9,11,12], infrared thermal imaging [13,14], and microwave scanning [15]. Numerical simulation was shown to be useful as well [16]. Of the listed techniques, X-ray, AE, and ultrasonics have been used extensively and reported widely. Ellingson et al conducted 84 experiments with samples made of ceramic composite. They fabricated their samples with various hidden defects. The authors tested the sample plates using several different nondestructive techniques including immersion phased array ultrasonics, transmission direct digital X-Ray imaging, scanning microwave, immersion single transducer scanning, ultrasound, and air coupled ultrasonics. They found phased array ultrasonic pulsing and X-Ray imaging to be the most cost and time effective [17]. Weight assembled the drawbacks and benefits of nondestructive techniques for testing armor for the techniques of acoustics/ultrasonics, thermography, holography and shearography, radiography, microwave, and computed tomography. They concluded that computed tomography to be the most advanced in comparison to the other types, but indicated these two advanced techniques are time consuming and expensive [18]. Margetan et al. manufactured their own armor plate prototypes (consisting of graphite epoxy, rubber, glass composite, ceramic, and then another glass composite) and tested them using a two transducer immersion pitch and catch system. They found that acoustic emission is effective at both finding and sizing delamination [11,19]. Richter et al. used time of flight in ultrasonic inspection to create simulation tools for inspection of multilayer armor [20]. Using 50 MHz pulse, they found their model could simulate the response of the layers and materials used as well as holding promise for future additions to the model. Grabowski at el. used time-distance transformation to locate an acoustic emission source in thin metallic plates [21]. The authors validated the ability to locate an AE source by using full AE waveforms and the basic geometry/material properties of the item being tested. A lead zirconate titanate transducers to excite flexural modes of the plates in the order of tens of kilohertz was reported in the work of Meitzler et al. [22]. The authors showed PZT transducers, in a variant of the impact method can characterize the resonant modes of vibration of a ceramic armor plate.

The usage of Acousto-ultrasonics (AU) to detect damage was reported for various structures and materials in a range of work [12]. The authors were able to distinguish the hidden defects from the received waveforms. This was because when a defect/damage is present, the wave interacts with the path changes therefore caused wave disruption. As a result, changes in terms of either dispersion or delay in the received waves indicated the presence of damage/defect. The authors showed a great potential for the detection of damage in composite structures and assessment of hard ballistic armor is ultrasonic guided waves.

In summary, there are five major methods used for nondestructive evaluation of body armor plates. The application and major advantages are listed as follows.

Thermography A heat source is applied to the surface of a material and the heat diffusion is tracked. Areas where there are defects or damage will cause the heat to not diffuse uniformly. From this, a schematic of the damage can be created. Temperature sensitivity decreases linearly with depth and deeper defects are not easily detected. *Radiography* A X-Ray or another energy source is used to create an image from the absorption of the particles. Sensitivity of this method is high and very useful in finding defects. This method can be limited as the fixture and equipment is bulky and not readily field accessible. *Microwave* Similar to radiography. Microwave energy is beamed onto the material and the backscatter is used to create an image. Microwave technology as a NDT method is rapidly advancing but currently has issues with conductive materials. *Computed Tomography* Computed Tomography uses either X-Ray or another energy source to scan a small slice of the material which is then digitally assembled to other slices until a model of the entire object is created. *Acoustics Emission, Ultrasonic, and Acousto Ultrasonics* Although there are many differences when using AE, Ultrasonics,

Preprints (www.preprints.org) | NOT PEER-REVIEWED | Posted: 31 October 2023 doi:10.20944/preprints202310.2048.v1

and AU, there is a common scenario such that they, in essence, cope with high frequency signals regardless the signals are artificially applied or generated passively from the tested articles. The signals transmit in the body and propagate through the materials under detection. The artificially applied signals can be either pulse echoed or have an opposing receiver. Many efforts have been reported in the field of damage evaluation of ballistic armor plates.

We tabulated the suitability and application of nondestructive evaluation of ballistic armor plates based on the reported work in Table 1.

Table 1. NDT Method Selection Category. An 'x' symbol means "not suitable".

	AE & Ultrosonics	Thermography	Radiography	Microwave	Computed Tomography
Multilayer	✓	x	✓	✓	✓
Cost-Effective	✓	✓	x	x	x
Portable	✓	✓	x	✓	x
Micro-level Detection	✓	x	✓	✓	✓
For large article	✓	x	✓	✓	x
For varied Materials	✓	x	✓	x	✓

In this table, NDT methods to evaluate armor plate are listed in the category of number of layers, cost effective, portable, micro-level detection, large plate compatible, and effectiveness for various materials. It can be seen that AE and ultrasonics method fit for all the categories. Over the years, AE and ultrasonics have been applied extensively and many successful achievements been reported [2,11,16]. However, waveform evaluation was employed in most AE related work, and ultrasonics studies were more involved in single layer materials. Therefore, the purpose of the present work is to develop a flight time based algorithm and to use commercial multilayered armor plates to demonstrate the proposed algorithm.

2. Materials and Methods

2.1. Test Samples and Instruments

TenCate graciously donated two commercially available body armor plates (Type IV) for our experiments. Figure 1 is a photo image of our sample test armor plate with dimensions of thickness about 50 mm (with the cover fabrics).

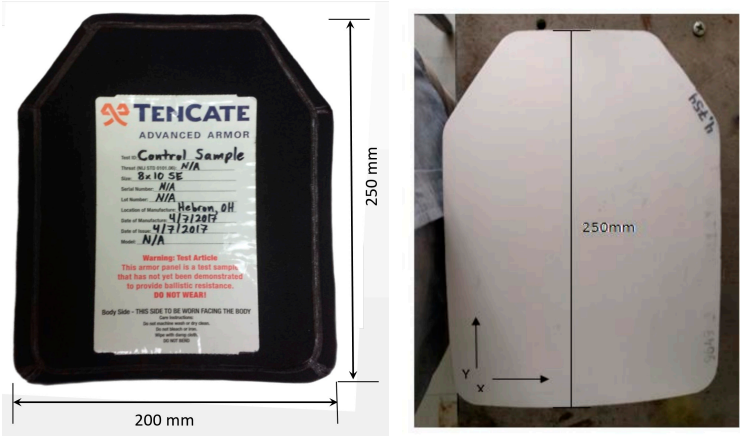

Figure 1. Geometry of control plate donated by donated by TenCate, Integris Composites Inc. **(a)** Armor plate with cover. **(b)** Defective plate with outer fabric removed.

Preprints (www.preprints.org) | NOT PEER-REVIEWED | Posted: 31 October 2023 doi:10.20944/preprints202310.2048.v1

A section view of the three different layers is shown in Figure 2. The top layer was ceramic, and the middle and bottom layers were made of a fiber/mesh material. The two bottom players are a material similar to Kevlar customarily made by TenCate. The detail compositions of the materials were not disclosed because of the intellectual property.

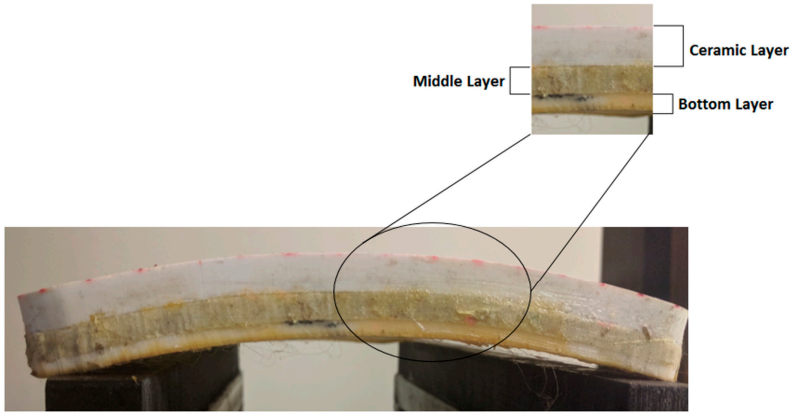

Figure 2. A section view of layer composition of the test samples donated by TenCate Advanced.

Of the two samples, one was used as the control sample with no defect, and the other had artificial defects built-in. While we provided a preliminary placement (Figure 3a) for TenCate to build the plate with defects on, they provided us the y-coordinates of each defect on the side of the defect sample, whereas the x- and z-coordinates (the layer where the defects were in) were blind to us. These defects were placed at the interfaces and then pressed into the layers during the manufacturing processes. The two balls of different sizes represent void type defects that may be introduced during the manufacturing, the wire segment (diameter around 1.0 mm) simulates a macro crack in the armor, while the 10.0 x 10.0 delaminated section would mimic when the armor layers separated due to improper construction or through usage. This "defective" ceramic armor plate provided items to scan for and allowed assessments to verify the soundness of the proposed algorithm.

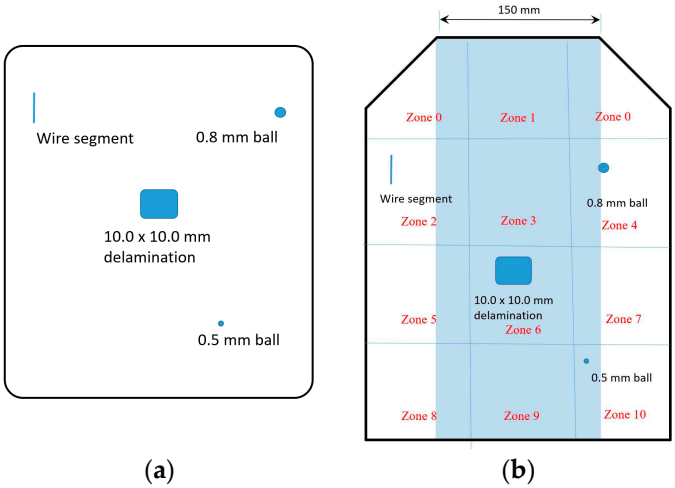

Figure 3. Types and zonal distributions of defects. (a) Types imbedded defects. (b) The shaded area complies with orthogonal measurement rules which will result reliable results, whereas there likely result undetectable or false detection due angle the path in longitudinal ultrasonic waves. The x locations of all the artificial defects were estimated.

For the purposes of comparison whether the artificial defects are visible to X-ray and to get a better idea of what would show up on the X-Ray versus what could be found when AU technique is used. We had both test samples to be subject to X-ray inspection after removing the cover fabrics as shown previously in Figure 2. An OrthoScan X-Ray low power generator ("OrthoScan: Imaging

Preprints (www.preprints.org) | NOT PEER-REVIEWED | Posted: 31 October 2023 doi:10.20944/preprints202310.2048.v1

Excellence," n.d.) was used. Because the dimension of the X-ray machine is limited, we partitioned the plate into different zones as shown in Figure 3b in order to map the imbedded defects in X-ray images. In this figure, the x-coordinates of the defects were labeled approximately based on the X-ray images since they were not given.

Notice that this armor plate is not in a full rectangle shape to promote an orthogonal measurements of longitudinal waves because of the chamfers at the top two corners. Because of the chamfers there exists an angle between pulsing and receiving sensors in the longitudinal wave such that orthogonal measurements are limited. The zones that fall completely in the shaded areas, 150 mm x 250 mm, are fully controlled which means orthogonal measurements can be achieved. Whereas zones have portions unshaded, it means that orthogonal measurements cannot be executed and, as a result, defects in these zones may not be detectable or may have false detection. However, this limit is fixable. Further discussions of non-orthogonal measurements are provided in the Discussion Section of this paper.

There was no identifiable defect in the control sample as expected. While, in the defective sample, the locations wire segment and 0.8 mm ball in Zones 1 and 3 were clearly seen as indicated in the zoomed windows in the callouts of Figure 4. However, the location of 0.5 mm was faintly identifiable according to the given y-coordinate, and the delamination was not identifiable.

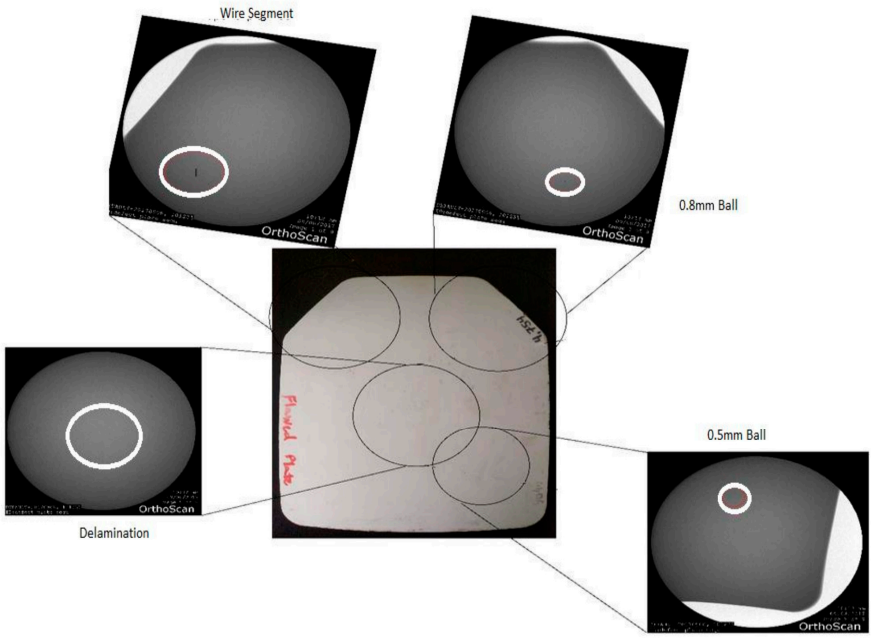

Figure 4. X-ray images of defective armor plate. Noticed that the smaller ball defect is dimly seen and no indication of the delamination.

For acousto-ultrasonics test, a Vallen Acoustic Software System (ASMY-5; Vallen-Systeme GmbH) was used. This system included: ASMY-5 AE data acquisition system and 40 dB pre-amplifier with a bandpass filter between 2.5 kHz and 3.8 MHz (AEP4; Vallen Systeme GmbH, Munich, Germany). To acquire the signals, we used piezoelectric AE sensors (Nano 30, Physical Acoustics, Inc., Princeton, NJ, USA). The resonant frequency and operating frequency range of these sensors are 140 kHz and 125–750 kHz, respectively, although the working frequency ranges anywhere from 30 kHz to over 800 kHz with a side lope covering 900 kHz to 1 MHz. This AE system was optimized to pulse at 10 MHz for our AU test, which allows at least 10-3 mm ideally and provides enough fidelity for the purpose of the present work [23]. The resultant AE signatures were pre-amplified by a 40 dB pre-amplifier with a bandpass filter between 2.5 kHz and 3.8 MHz (AEP4; Vallen Systeme GmbH, Munich, Germany) before being fed to the AE system. The threshold for the data acquisition was selected to minimize the noise from the testing machine, this being done by installing the specimen

Preprints (www.preprints.org) | NOT PEER-REVIEWED | Posted: 31 October 2023 doi:10.20944/preprints202310.2048.v1

on the testing machine with near zero loading and finding that there were no detectable acoustic signals at or below 35.5 dB. Thus, this value was used as the threshold.

2.2. Flight-Time Matrix

Flight time, in this work, is defined as the time needed for a pulsing longitudinal ultrasonic wave to travel from the pulser transducer to the receiver transducer. In a 2D testing object, let t_{xi} and t_{yj} be the flight time in the x- and y-directions, respectively. They is determined as follows,

$$\boldsymbol{t_{xi} = (t_r - t_p)|_{xi}}, \text{for } \boldsymbol{i = 1, 2, \cdots, N} \tag{1}$$

$$\boldsymbol{t_{yj} = (t_r - t_p)|_{yj}}, \text{for } \boldsymbol{j = 1, 2, \cdots, M} \tag{2}$$

where, t_r and t_p are the time at the pulser and receiver transducers, respectively. x_i and y_j are the x- and y-coordinates at which an ultrasonic longitudinal wave is pulsed, and N and M are the indices in x- and y-coordinates of the testing objects, respectively.

In Equations (1) and (2), it can been seen that flight time is a difference between the time at the receiver and that at the pulser transducers. When executing $\boldsymbol{i = 1, 2, \cdots, N}$ and $\boldsymbol{j = 1, 2, \cdots, M}$, the testing object is in essence partitioned which creates mesh. The measurements of flight times are thus obtained in x- and y-direction accordingly. The results of these measurements are in two arrays: $\boldsymbol{T_x}$ and $\boldsymbol{T_y}$. Similarly, in the cases of 3D object, $\boldsymbol{T_z}$ is the flight time in z-coordinate. Graphs of $\boldsymbol{T_x}$, $\boldsymbol{T_y}$, and $\boldsymbol{T_z}$ are able to show the variations of flight time in the x-, y-, and z-directions individually. These graphs reveal the corresponding linear position of damage/defect that causes the flight time delay, which had been used mostly [25].

If $\boldsymbol{T_x}$ and $\boldsymbol{T_y}$ are used to construct a matrix according to an algorithm, a flight time matrix can be formed. We propose a novel algorithm that can be used to construct such a matrix using the 1D flight time arrays, and define it to be the flight time matrix (FTM) in this work. This proposed algorithm is described in Equation (3) mathematically. Elements of FTM,

$$\boldsymbol{FTM(t_{xi}, t_{yj}) = t_{xi} + t_{yj},\ for\ i = 1, 2, \cdots N}; \text{and } \boldsymbol{j = 1, 2, \cdots M} \tag{3}$$

In this matrix, the unit of each element is time, which means the time needed to travel from the pulser to the receiver. FTM is, in essence, a collection of the time needed for the high frequency wave to travel from the pulser to the receiver. The greater the value of an element in FTM, the longer the time that a longitudinal wave travels. The occurrence of a significant large value of flight time can be highly attributed to the facts of the presenting damage/defect that may have changed/altered the passage of an ultrasound wave. Although N and M are the indices of FTM in a 2D testing object, they have physical meanings as the follows. These indices create a grid mesh on the testing body, the finer the mesh, the higher the resolution of the measurements, and the more accurate the results. The determination of N and M is dependent on a number of factors such as the physical size of the pulser and receiver transducer, the physical size of a testing object, the expected resolution, and others like the time period to complete an evaluation. The purpose of constructing a FTM is that the contour graphs of this matrix will provide a better visualization of the damage occurred in an object. The unit of FTM is the time, and depending on the size of a testing object, it can be s, ms, or ns. However, a normalized time is used to be time/length because the physical size of a testing object is often different in x, y, and z directions.

We shall describe means to construct 2D FTM in this work, a 3D FTM can be followed in a similar token. A ballistic armor plate is a typical 2D testing object as the thickness of an armor plate is far less than the length and width of the surface area. Table 2 shows the construction of a 4x3 FTM.

Preprints (www.preprints.org) | NOT PEER-REVIEWED | Posted: 31 October 2023 doi:10.20944/preprints202310.2048.v1

Table 2. Method of light Time Matrix (FTM) construction for a 4x3 resolution of a FTM.

	t_{X1}	t_{X2}	t_{X3}	t_{X4}
t_{Y1}	$t_{X1}+t_{Y1}$	$t_{X2}+t_{Y1}$	$t_{X3}+t_{Y1}$	$t_{X4}+t_{Y1}$
t_{Y2}	$t_{X1}+t_{Y2}$	$t_{X2}+t_{Y2}$	$t_{X3}+t_{Y2}$	$t_{X14}+t_{Y2}$
t_{Y3}	$t_{X1}+t_{Y3}$	$t_{X2}+t_{Y3}$	$t_{X3}+t_{Y3}$	$t_{X4}+t_{Y3}$
t_{Y4}	$t_{X1}+t_{Y4}$	$t_{X2}+t_{Y4}$	$t_{X3}+t_{Y4}$	$t_{X4}+t_{Y4}$

FTM can be formed in different means, for instance, depending on the pulse orientation, an FTM can be constructed as follows:

- Solo-orientation. The pulser and receiver positions are fixed, meaning that the longitudinal wave propagates in a unidirectional way; and,
- Dual-orientation. The pulser and receiver positions are exchanged, meaning that longitudinal wave propagates in one direction first, and reversed.

2.3. Numerical Simulation

We generated two arrays, $\boldsymbol{T_x(n)}$ and $\boldsymbol{T_y(m)}$ of normal distribution to represent orthogonal measurements of flight time where $\boldsymbol{n = 20}$ and $\boldsymbol{m = 25}$. FTM was then established based on Equation (3). To simulate and compare the presence of defects, two numerical scenarios were created: measurements with no defects and measurements with defects. Method to create defect was described as follows.

Let the location of a defect be at $\boldsymbol{x = 10}$ and $\boldsymbol{y = 8}$, and the standard deviations of $\boldsymbol{T_x(n)}$ and $\boldsymbol{T_y(m)}$ be $\boldsymbol{\sigma_x}$ and $\boldsymbol{\sigma_y}$. Assume the value of flight time may increase 2 times of its standard deviation at location of (10, 8), such that,

$$\boldsymbol{T_x(10)|_{new} = T_x(10) + 2\sigma_x} \text{ and } \boldsymbol{T_y(8)|_{new} = T_y(8) + 2\sigma_y} \quad (4)$$

where $\boldsymbol{2\sigma}$ is used as the increase of the flight time due to the presence of a defect. This value was an estimation for numerical simulation.

2.2. Test Method

We tested each layer individually as their thickness is sufficient to cope with the transducer. Two transducers were placed face-to-face on the side of each layer in the armor plate: one pulsing and one receiving. However, due to the chamfered edges of the armor plate, as shown in Figure 5, there are zones where orthonormal longitudinal waves are not applicable. In this figure, areas that can promote orthogonal longitudinal waves are the shaded ones where the transducers are in the line of sight with each other. The zones that are partially shaded will result failures or misdetection of our methods due to the angle of the plate were limited.

The increment of measurement was the size of the transducer diameter, 8.0 mm. We pulsed 10 times at each location and collected the time of flight in both x- and y-directions. Sil-Glyde Lubricating Compound was applied to the face of the transducers to insure a good contact between the transducer/plate interfaces. The steps of testing method is given in the following:

- *Measurement* measure the flight time on x- and y-coordinate, respectively, according to a predetermined the increment of 8.0 mm.
- *Construction of FTM* Construct $\boldsymbol{T_x}$, $\boldsymbol{T_y}$, and FTM arrays based on Equations (1)–(3).
- *Graphic Analysis* Analyze the flight time plots and FTM for flight time spikes and color intense locations.

Preprints (www.preprints.org) | NOT PEER-REVIEWED | Posted: 31 October 2023 doi:10.20944/preprints202310.2048.v1

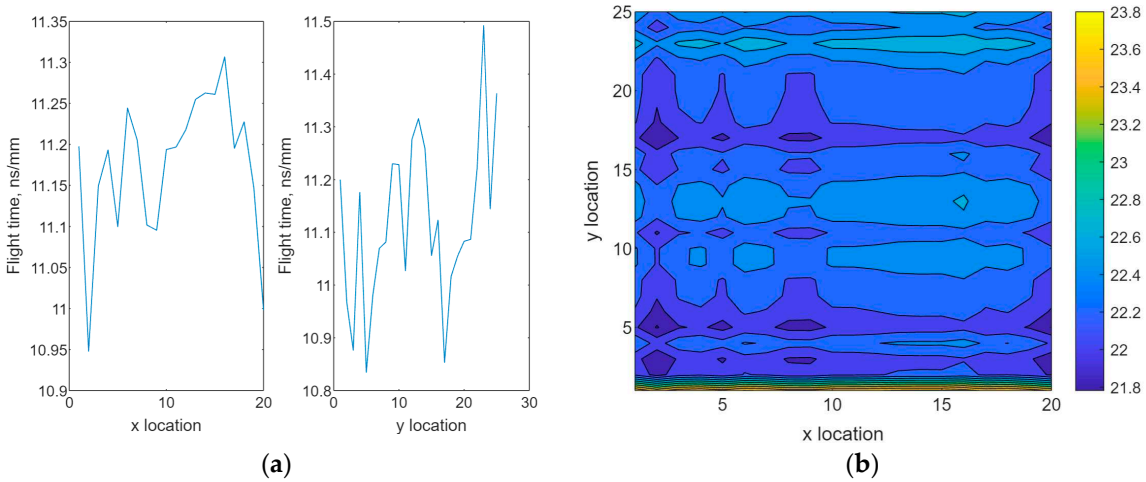

Figure 5. Flight times and defect location when there is no defect. **(a)** Flight time vs. x- and y-coordinates, respectively. Note that the values of flight time have been normalized to eliminate the size effect, thus the unit of flight time is unit per mm. **(b)** FTM contour plot.

3. Results

3.1. Results of Numerical Simulation

The simulated results of flight time in x- and y-directions based on Equation (4) is shown in Figure 5. As it is expected there are no major flight time spikes except for the random fluctuation in the data.

A contour plot of FTM with no defect included. It can be seen that there are no color intense regions as it will be compared with the defect added. Some relatively color intensed regions were due to the randomness of the simulated data.

When defect was added to the simulated data as described in Equation (4) at the location of $\boldsymbol{x = 10}$ and $\boldsymbol{y = 8}$, the flight times in x- and y-directions are revealed in Figure 6a,b. It clearly observed that spikes are present in the graphs of flight time vs locations.

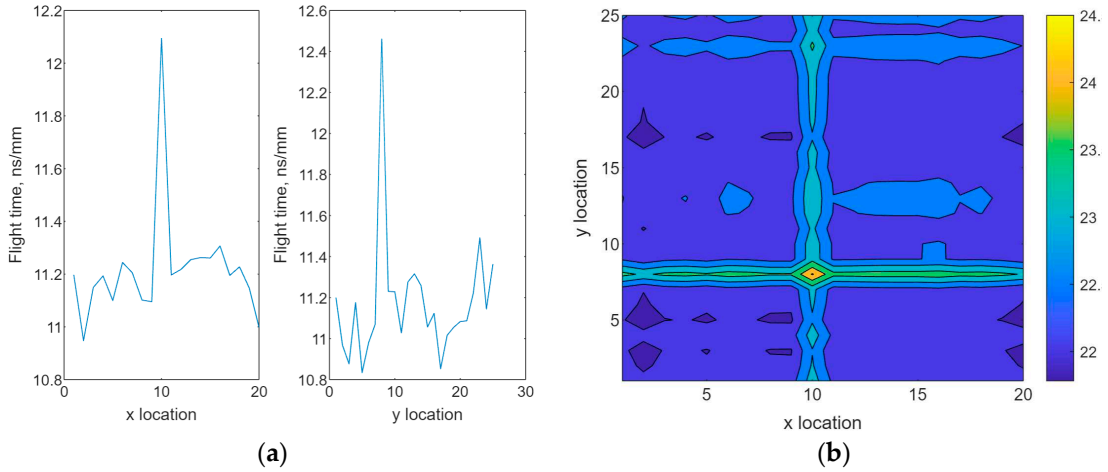

Figure 6. Similar to Figure 5, but a 2σ defect was added. **(a)** Flight time vs. x- and y-coordinates, respectively. **(b)** FTM contour plot.

3.2. Experimental Results

To test the concept of FTM, we took a rectangle Plexiglas plate as an evaluation target to identify its response to our FTM algorithm. It showed excellent results that our algorithm can be a good means to handle hidden defects in materials. To limit the pages, readers who may have interests are referred to Tankersley's MS thesis [9].

Preprints (www.preprints.org) | NOT PEER-REVIEWED | Posted: 31 October 2023 doi:10.20944/preprints202310.2048.v1

Of the case study with TenCate ballistic armor plates, the flight time of each ultrasound pulse was collected for each layer (ceramic, middle, and bottom) in both x- and y-direction. The entire armor plate, x = 200 mm and y = 250 mm, was scanned by pulsing longitudinal waves in both x- and y-directions, respectively. Notice that the fully controlled area of 150 mm x 250 mmm as shown in Figure 3b. Results presented in this section were based on the data from the fully controlled area only.

The flight time values in each of x- and y-direction were normalized by the distance traveled to eliminate the effect of distance while maintain its orthogonal properties. The normalized flight time value is, actually, the unit of per mm. A corresponding FTM was constructed for each layer [9]. The normalized minimum and maximum time of flight for each layer on both plates was tabulated in Table 3.

Table 3. Statistics of Flight Time.

		Control Plate	Defective Plate
Ceramic Layer	Min FT	11.160	11.320
	Max FT	11.740	12.000
	FT Range	0.580	0.680
Middle Layer	Min FT	14.225	14.960
	Max FT	16.620	20.170
	FT Range	2.395	5.210
Bottom Layer	Min FT	12.240	12.130
	Max FT	12.780	12.770
	FT Range	0.540	0.640

In this table, the average of minimum and maximum FT, and difference of FT for each layer were listed. Because of the different materials of each layer, the statistics are different. However, some interesting facts were noticed from this table:

- There were no significant variation in the control and defective plates when comparing the data between the ceramic and bottom layers' data; whereas,
- There is a significant changes in the middle layer where FT range is almost double that in the defective plate comparing to that in the control plate.

Figures 7–9 are the views by superimposing the FT in x-and y-directions array data and the contour plots of FTM for the control plate.

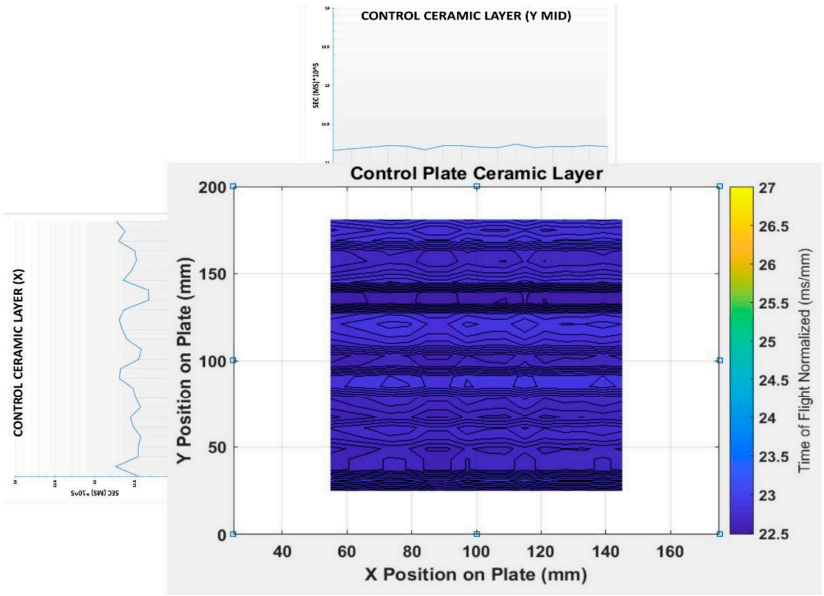

Figure 7. Ceramic layer of FTM for control plate contour plot.

Preprints (www.preprints.org) | NOT PEER-REVIEWED | Posted: 31 October 2023 doi:10.20944/preprints202310.2048.v1

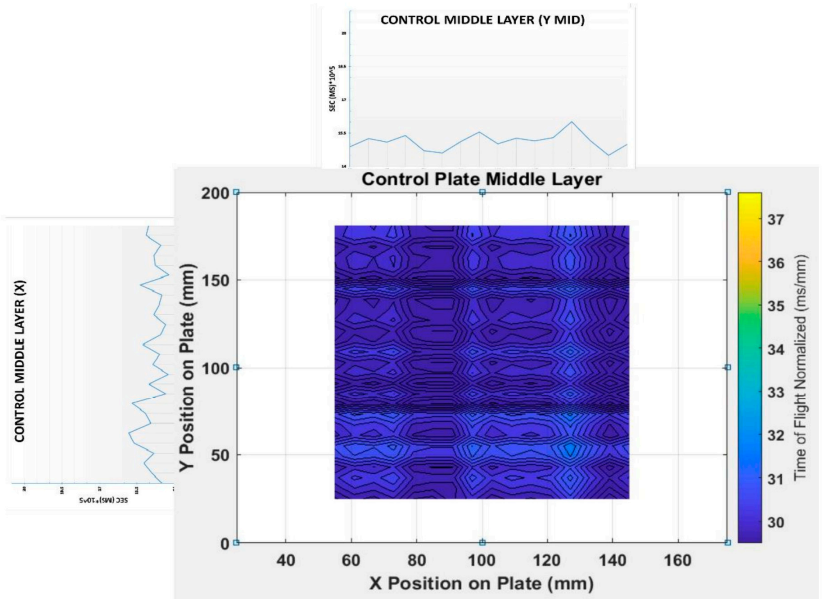

Figure 8. Middle layer of FTM for control plate contour plot.

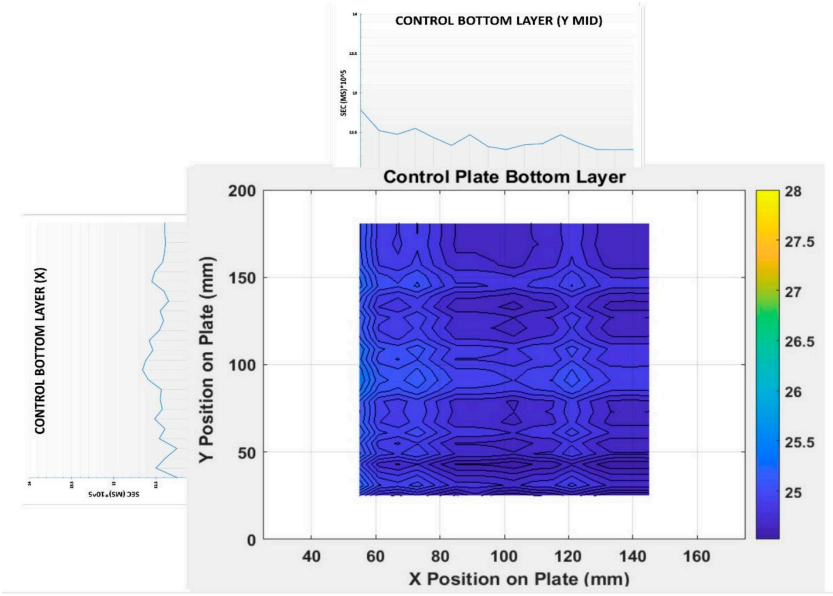

Figure 9. Bottom layer of FTM for control plate contour plot.

In these figures, there are no intense variations in color changes which means that there is no significant changes in the statistics of FT values, therefore defects are less likely present. Similar images are found for the ceramic layer and bottom layer of defective plate correspondingly, which can be referred to the work of Tankersly [9]. It is the Figure 10 that got our attention: the intense variations in color grade and the flight time spikes in both x- and y-directions in the middle layer for the defective plate. The flight time in both x- and y-directions and 2D contour plot were superimposed as before.

Preprints (www.preprints.org) | NOT PEER-REVIEWED | Posted: 31 October 2023 doi:10.20944/preprints202310.2048.v1

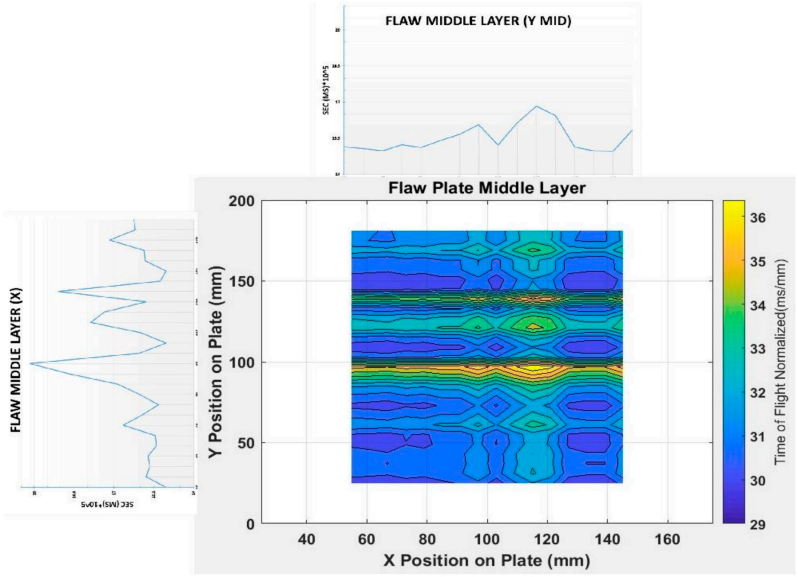

Figure 10. Middle layer of FTM for defective plate contour plot.

It can be seen that the color intense point (36 ns/mm) is centered at around x = 110 mm and y = 98 mm. It is therefore the location of 0.5 mm defect, which can be assured by the given y-coordinate of this small hole. The horizontal color intense line regions at a small neighborhood of y = 98 mm and a small neighborhood of x = 110 mm are due to the superposition when constructing FTM. The delamination was found around the location of x = 95 mm and y = 115 mm (given) where 34.5 ns/mm on the contour scale, although it is not very clear. An interesting fact was found that at around y = 145 mm there is another color intense region, whereas y = 145 mm is the given location of the 0.8 mm hole. From this figure, it can be seen that it barely formed a color intense region at the edge in this figure. We can firmly presume x = 145 mm is the location of 0.8 mm hole. To summarize, Figure 11 is a simple FTM contour plot that shows the defects labeled.

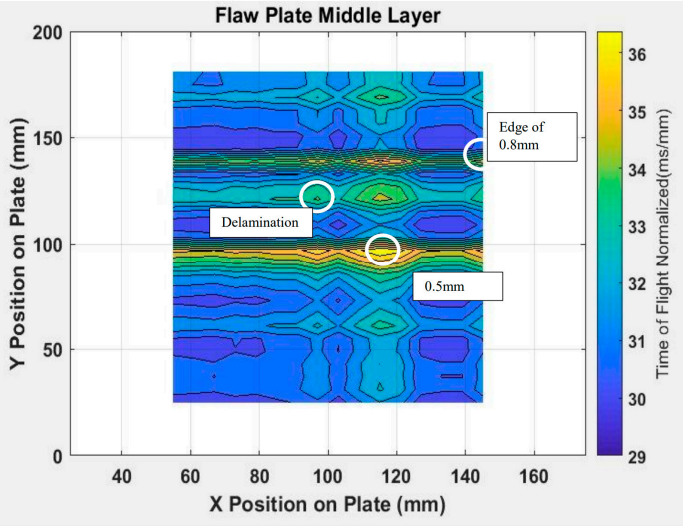

Figure 11. The same as that in Figure 9, but without superimposition in x and y fight time.

4. Discussion

In the present work, there are well controlled zones in which the defects were detected accurately. However, the wire segment is not detected because it located completely outside the controlled the region. It can be deduced orthogonal measurement is a necessary condition. Under

 doi:10.20944/preprints202310.2048.v1

such a condition, a orthonormal grid both in x- and y-directions is required to secure the detection of a defect location in 2D.

This brings a noteworthy point: when the testing object is not in rectangular shape to promote such an orthogonal grid to promote the measurements, an answer may not exist or misdetection may occur. However, this is a solvable problem. Orthogonal measurements can be proceed by taking additional actions, for instance, use of a waveguide to direct the longitudinal wave path. This way the longitudinal wave path can be prolonged whenever needed to establish the orthogonality. Other methods may also be taken to assist the formation of required orthogonality. We shall report our future efforts that overcome the testing objects which do not promote orthonormal FTM.

5. Conclusions

In this work, a novel concept of FTM (flight time matrix) algorithm is developed and the means to construct a FTM is described in detail. We tested FTM first by a numerical simulation of flight time measurements. The numerical simulation revealed perfect results which showed that FTM can be used to assist the nondestructive evaluation of ballistic armor plate using acousto-ultrasonics. The experimental results of flight time and FTM were reasonably well. The artificial defects were clearly identifiable in one directional location array and FTM contour plots. More comprehensive superimpositions of flight time vs location and FTM contour plots can be advanced to a better visualization of the defect presence. The resolution of FTM method can be in the range of submillimeter or less. This study demonstrated that AU (acousto-ultrasonics) technique is a field applicable and yet reliable tool for inspection of the hidden defects in body armors.

A broader merit of our FTM algorithm is that it may also promote the development of specific tools/device for nondestructive evaluations field.

References

1. Mehara, M., Goswami, C., Kumar, SR. et al, “Performance evaluation of advanced armor materials,” Materials Today: Proceedings, vol. 47(17), pp. 6039-6042, 2021.
2. Marks, R., Grigg, S., Crivelli, D. Pullin R. et al, “Development of an automated assessment technology for detecting damage in body armour,” J. Mechanical Engineering Science, vol. 234, 2020..
3. Roberson, C. Roberson, G. P. et al, in Personal Armour Systems Symposium. International Personal Armour Committee (IPAC), Leeds, UK. 2006.
4. Miller, L., “Selection and application guide to personal body armor (NIJ Guide 100–01),” US Dep Justice, Natl Inst Justice’s Natl Law Enforc Correct Technol Center, Washington, DC.
5. Wikipedia, “List of body armor performance standards,” 10 September 2023. [Online]. Available: https://en.wikipedia.org/wiki/List_of_body_armor_performance_standards.
6. Li, G., Wang Z., and Yang, L. “Non-Destructive X-ray Evaluation and Gap Measurement of Ceramic Armor Plate, ” J. Phys.: Conf. Ser..
7. Chiou, C.-P., Margetan, F. J., “Nondestructive characterization of UHMWPE armor materials,” in AIP Conf. Proc, 2012.
8. Lovea, M., Cerit, M. and Tunç, A., “Development of a non-destructive testing system for the automated inspection of ceramic armour plates and parts,” in AIP Conf. Proc., 2012.
9. Tankersly, S. J., “Evaluation of Damage in Multilayered Armor Plates Using Acousto-Ultrasonics,” The University of Memphis, Memphis, TN 38152, 2019.
10. Woo, S.-C., Kim, J.-T., Kim, J.-Y., “Correlation of fracture processes and damage mechanisms of armor structural materials under high strain rates with acoustic emission characteristics,” International Journal of Impact Engineering, vol. 63, pp. 29-42, 2014.
11. Margetan, F., Richter, N., Barnard, D., et al., “Baseline UT measurements for armor inspection,” in AIP, 2010..
12. Loendersloot, P., Moix-Bonet, M., “Damage identification in composite panels using guided waves,” in Proceedings of the 5th CEAS Air & Space Conference., 2015.
13. Johnston, J. P., Pereira, J. M., Roberts, G. D., “High-speed infrared thermal imaging during ballistic impact of triaxially braided composites,” Journal of Composite Materials, vol. 52(25), 2018.

14. Feng, F.Z., "Identification and Reconstruction of Cracks in Ultrasonic Infrared Thermography," Applied Mechanics and Materials, Vols. 249-250, 2013.
15. Schmidt, K., Little, J., Ellingson, W., "A Portable Microwave Scanning Technique for Nondestructive Testing of Multi layered Dielectric Materials," Advances in Ceramic Armor, vol. 29(6), 2009.
16. Alkhatib, F., Mahdi, E. Dean, A., "Design and Evaluation of Hybrid Composite Plates for Ballistic Protection: Experimental and Numerical Investigations," Polymers, vol. 13(9), p. 1450, 2021.
17. Ellingson, W., Koehl, E., Meitzler, TJ., Franks, L. et al, "A Comparison of NDE Methods for Inspection of Composite Ceramic Armor. Adv Ceram Armor VI," in Adv Ceram Armor VI Ceram, 2010.
18. Weight, K., "An Overview of NDE Methods for Thick Composites and a Proposal for," Army Research Lab, Watertown MA. Materials, 1994.
19. Margetan, F., Richter, N., Jensen, T. et al, "Porosity detection in ceramic armor tiles via ultrasonic time-of-flight," in AIP, 2011.
20. Richter, N., FJ., Margetan, Gray, T. et al, "Simulation tools for ultrasonic inspections of multi-layer armor panels," in AIP, 2011.
21. Grabowski, K., Gawronski, M., Baran, I. et al, "Time-distance domain transformation for Acoustic Emission source localization in thin metallic plates," Ultrasonics, vol. 68, pp. 142-149, 2016.
22. Meitzler, T., Smith, G. Charbeneau, M., "Crack detection in armor plates using ultrasonic techniques," Mater Eval, vol. 66(6). 2008.
23. US Airforce and US Navy, "NONDESTRUCTIVE INSPECTION METHODS, BASIC THEORY," in TECHNICAL MANUAL, 2014.
24. Thomas, EL., "Opportunities in Protection Materials Science and Technology for Future Army Applications," in Advances in Ceramic Armor VIII, Wiley, 2012, pp. 145-148.
25. Espinosa, Luis; Bacca, Jan; Prieto, Flavio; Lasaygues, Philippe; Brancheriau, Loïc, Accuracy on the Time-of-Flight Estimation for Ultrasonic Waves Applied to Non-Destructive Evaluation of Standing Trees: A Comparative Experimental Study. Acta Acustica united with Acustica, 104(3), 2018, pp.429-439.